Design of Inversion Procedure for the Airborne CO_2-IPDA LIDAR: A Preliminary Study

Chengzhi Xiang, Xin Ma, Xingying Zhang, Ge Han, Wanchun Zhang, Binglong Chen, Ailin Liang, and Wei Gong

***Abstract*—China will launch the atmospheric environment monitoring satellite, which is equipped with a CO_2-integrated path differential absorption (IPDA) LIDAR, in the coming years. The space-borne IPDA LIDAR is believed to supplement current passive remote sensing techniques in terms of effective observations at nights, as well as in high-latitude regions and heavily polluted areas. Currently, no LIDAR-based satellite is operational for CO_2 detection in orbit despite the fact that Active Sensing of CO_2 Emissions over Nights, Days, and Seasons (ASCENDS) and Advanced Space Carbon and Climate Observation of Planet Earth (A-SCOPE) are dedicated to fill this gap. However, the ESA mission proposal A-SCOPE dedicated for CO_2 measurement was not selected, and ASCENDS from NASA remains in the loop but on low priority. Therefore, it is of great significance to explore the feasibility and effectiveness of this novel technique and to identify potential differences among its CO_2 concentration products and the passive remote sensing technique. In this article, we developed an initial data-processing procedure for an airborne CO_2-IPDA LIDAR, which is the minified prototype of the forthcoming space-borne LIDAR. We tested the effectiveness of this procedure and evaluated the performance of the minified prototype in a flight test over ocean, urban, and mountainous terrain. The column-weighted xCO_2 (XCO_2) retrievals obtained by the airborne IPDA LIDAR were considerably more sensitive to the gradients of the dry-air mixing ratio of CO_2 (xCO_2) than the XCO_2 products of OCO-2 and *in situ* measurements of point xCO_2. The mean XCO_2 values over the ocean, urban, and mountainous area were 411.07, 425.71, and 417.87 ppm with STDs of 1.93, 0.85, and 0.96 ppm, respectively. We used altitude-dependent xCO_2 obtained by a decline-climb flight to calculate a reference for XCO_2 over the ocean. The difference between XCO_2 obtained using two means was less than 0.5 ppm. Moreover, the actual random error coincided well with the simulated random error, suggesting that our previous performance-evaluation model was reliable. This model predicted that a relative random error of less than 0.3% would be very likely for the forthcoming satellite mission over land. However, measuring CO_2 concentrations precisely over oceans was identified as a very challenging work. Improvements in hardware technology are unlikely to narrow this gap largely. Thus, developing dedicated algorithms to address CO_2 measurement over oceans by using IPDA LIDAR is necessary.**

***Index Terms*—CO_2 concentration, data processing, integrated path differential absorption (IPDA) LIDAR, preliminary study.**

Manuscript received August 19, 2021; revised October 16, 2021 and November 2, 2021; accepted November 2, 2021. Date of publication November 12, 2021; date of current version December 1, 2021. This work was supported in part by the Natural Science Foundation of Jiangsu Province, China under Grant BK20180809 and Grant BK20190779; in part by the National Natural Science Foundation of China under Grants 41901274, 42171464, 41971283, 42001273, 41801261, 41801282, 41775028, and 41827801; in part by the Talent Launch Fund of Nanjing University of Information Science and Technology under Grant 2017r066; in part by the National Key R&D Program of China under Grant 2017YFB0504001; in part by the Open Research Fund of National Earth Observation Data Center under Grant NODAOP2021005; and in part by the General Projects of Natural Science Research in Colleges and Universities of Jiangsu Province under Grant 19KJB170021. *(Corresponding authors: Xin Ma; Ge Han.)*

Chengzhi Xiang and Ailin Liang are with the School of Remote Sensing and Geomatics Engineering, Nanjing University of Information Science and Technology, Nanjing 210044, China (e-mail: xcz0726@nuist.edu.cn; ireneliang@nuist.edu.cn).

Xin Ma is with the State Key Laboratory of Information Engineering in Surveying, Mapping and Remote Sensing, Wuhan University, Wuhan 430072, China (e-mail: maxinwhu@gmail.com).

Xingying Zhang is with the Key Laboratory of Radiometric Calibration and Validation for Environmental Satellites, National Satellite Meteorological Center, China Meteorological Administration, Beijing 100081, China, and also with the FengYun Meteorological Satellite Innovation Center, Beijing 100081, China (e-mail: zxy@cma.gov.cn).

Ge Han is with the School of Remote Sensing and Information Engineering, Wuhan University, Wuhan 430072, China (e-mail: udhan@whu.edu.cn).

Wanchun Zhang and Binglong Chen are with the Key Laboratory of Radiometric Calibration and Validation for Environmental Satellites, National Satellite Meteorological Center, China Meteorological Administration, Beijing 100081, China (e-mail: zhangwc@cma.gov.cn; chenbl@cma.gov.cn).

Wei Gong is with the School of Electronic Information, Wuhan University, Wuhan 430072, China (e-mail: weigong@whu.edu.cn).

Digital Object Identifier 10.1109/JSTARS.2021.3127564

I. Introduction

THE INCREASE in anthropogenic carbon emissions since the industrial revolution has led to considerably elevated atmospheric CO_2 concentrations and is considered as an important contributor to climate change [1]. To understand the distribution and dynamics of carbon sinks and sources and develop reasonable climate-change-mitigation measures, scientists estimate CO_2 fluxes by measuring atmospheric CO_2 concentrations [2]–[4]. Given that the current ground-based observation network is too sparse to limit the inversion of high-resolution CO_2 fluxes, researchers rely on satellite observations to provide additional information at a global scale by using dense CO_2 concentrations [5]. Thus, over the last decade, increasing number of satellite missions dedicated to CO_2 observations such as GOSAT-1/2, OCO-2/3, TanSat, GF-5, and FY-3D has increased [6]–[10]. The novel data provide insights into the carbon cycle and climate change [11]–[14]. However, these missions cannot obtain effective observations at high latitudes, at night, in heavy pollution, and under cloudy conditions owing to the intrinsic shortcomings of the passive remote sensing technique [15], [16]. For example, the short-wave infrared detectors primarily rely on the solar radiation reflected from the ground, so it can work only at daytime or even at high-solar-altitude angles. CO_2-concentration information is also difficult to gather at high latitudes. A thermal

infrared detector uses thermal infrared radiation to perform atmospheric CO_2 detection, whereas the radiation of ground and lower atmosphere in the thermal infrared band is very similar. Thus, it can obtain the CO_2 concentration information only in the middle and upper atmospheres and is very insensitive to the CO_2 concentration in the atmosphere at the bottom of the troposphere. The interferences of aerosol and cloud are also difficult problems that cannot be overcome by passive remote sensing technique [17], [18].

To complement existing passive remote sensing means, several countries are competing to develop new approaches to measure atmospheric CO_2 concentration by using LIDAR [19]–[23]. ESA and NASA have proposed the Advanced Space Carbon and Climate Observation of Planet Earth (A-SCOPE) and Active Sensing of CO_2 Emissions over Nights, Days, and Seasons (ASCENDS) plan, respectively. A-SCOPE is one of the six candidate Earth Explorer Missions selected by ESA. This mission focuses on the determination of regional carbon source and sink and uses the inversion model to detect atmospheric CO_2 through CO_2 absorption in the near-infrared region [24], [25]. ASCENDS is a space-borne CO_2-detection program initiated by NASA. NASA's Goddard Space Flight Center has developed a multiwavelength pulsed integrated path differential absorption (IPDA) LIDAR technology and conducted the first airborne CO_2 IPDA LIDAR experiment [15]. More airborne CO_2-IPDAs have been conducted by different research groups in the following years [26]. Several simulation studies have demonstrated the promising performances of these ongoing missions [27]–[29]. Similar to what NASA and ESA have already performed for their ASCENDS and A-SCOPE missions, China needs to conduct practical tests of its space-borne CO_2-IPDA LIDAR, which is currently under development [30], before it is launched because of the imperfect performances of the country's existing CO_2-observation satellites [22], [31], [32].

A collaborative flight test organized by several institutions was performed in spring 2019. This test had the crucial task of testing the performance of the CO_2-IPDA LIDAR through real experiments and to provide meaningful data for the validation and evolution of algorithms for retrieving the CO_2 column-weighted dry-air mixing ratio. Meanwhile, the design and number of flight tests are constrained by strict aviation regulations and high costs, and comprehensive sensor tests are unlikely to be completed in a single-series experiment. However, this flight test represents a precious opportunity for testing and improving our performance-evaluation model such that outcomes with increased reliability can be expected in the future. A minified prototype of the space-borne CO_2-IPDA LIDAR was developed for this mission. In the present article, we reported the results obtained from that flight test. The main idea was to evaluate the precision and sensitivity of the minified prototype. Moreover, the dependence of performance on land cover was presented. Using our simulation model of performance as a medium, we further mapped the performances of the minified CO_2-IPDA LIDAR to those of the ongoing space-borne version of CO_2-IPDA LIDAR.

At the end of the introduction part, we clarify several abbreviations regarding the definition of CO_2 concentration. In this article, xCO_2 represents the dry-air mixing ratio of CO_2, which is often obtained by *in-situ* measurement approaches and is a description of point concentration. XCO_2 represents column-average xCO_2, which is the typical product of OCO-2 or a ground-based Fourier transform infrared spectrometer (FTIR). For customary reasons, we still use XCO_2 to represent column-weighted xCO_2 in this article. But it is noting that column-average xCO_2 and column-weighted xCO_2 are similar but different concepts. In Section II, we provide the mathematical definition of column-weighted xCO_2. In actuality, an airborne IPDA LIDAR measures partial XCO_2 because a plane does not fly outside the atmosphere. However, in this article, we do not distinguish between partial XCO_2 and XCO_2 explicitly unless we simultaneously discuss space-borne IPDA LIDAR and airborne IPDA LIDAR.

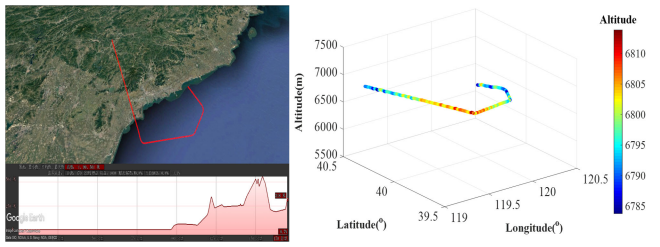

Fig. 1. Test area and trajectory of the flight campaign. The left figure is the trajectory as seen from Google Earth with ground elevation, and the right figure is the altitude change of the aircraft. The flight path was basically flat, and the average altitude, maximum altitude, and minimum altitudes of the aircraft were 6796, 6814, and 6769 m, respectively.

The remaining parts of this article are arranged as follows. In Section II, the basic theory of an IPDA LIDAR, information on flight tests, and the multiple types of data used in this article are described. In Section III, we report the main results, including received laser signals, XCO_2 retrievals, and comparisons with *in-situ* measurements and OCO-2 XCO_2. Subsequently, we compare results from real experiments and simulations of our performance model and discuss the implications of this flight test in future satellite campaigns in Section IV. Finally, Section V concludes this article.

II. Methodology

A. Flight Campaign

The airborne atmospheric carbon dioxide LIDAR (ACDL) system was completed and commissioned in August 2018, and a flight campaign was conducted in Shanhaiguan, China, in March 2019. The flight altitude was approximately 7 km. The airborne ACDL system comprised a laser transmitter, instrument control, environmental control, and LIDAR transceiver subsystem. More details of the system are described in Appendix A.

The route of the flight campaign passed ocean, plain, and mountainous areas to measure the CO_2 concentration information of different underlying surfaces. The aircraft flew from the seaside to the ocean and then across plains toward a mountainous area. The trajectory of the flight analyzed in this article is shown in Fig. 1. The flight time was from 11:15:39 to 11:39:24 on March 14, 2019.

B. Data Sources

We evaluated the precision and sensitivity of the airborne ACDL system through a series of data analyses and comparisons. Data sources primarily included ACDL detection data and OCO-2 data. The ACDL detection data included LIDAR echo signals, inertial navigation information, temperature, humidity and pressure data, and *in-situ* CO_2 analyzer data. OCO-2 data primarily adopted atmospheric CO_2 column concentration information for the same time and areas.

1) ACDL Detection Data: Inertial navigation information: The inertial navigation system primarily monitored the attitude information of the aircraft to ensure that the CO_2 column concentration in the vertical direction could be accurately measured even when the aircraft was shaking. The attitude information provided by inertial navigation included the following: yaw angle, pitch angle, roll angle, latitude, longitude, altitude, east speed, north speed, and vertical velocity. The time information was GPS week and GPS second.

Temperature, humidity, and pressure data: The temperature, humidity, and pressure data on the detection path were primarily used to calculate the CO_2 weight function. In this campaign, the AIMMS-20 sensor, which was produced by Aventech, was used to measure the temperature, humidity, and atmospheric pressure on the flight path.

CO_2 *in-situ* measuring instrument: An LGR ultra-convenient greenhouse gas analyzer was placed in the cabin of the aircraft to measure the CO_2 concentration information at the flight altitude of the aircraft to compare and verify the CO_2 concentration data measured by LIDAR.

Camera: A color CMOS camera was placed next to the LIDAR telescope for the ground observation of underlying surface types.

2) OCO-2 Data: OCO-2 is a special passive CO_2 detection satellite with high detection accuracy [33]–[36]. In this article, the XCO_2 detected by OCO-2 at the same time and area was used for comparative analysis, which could enable a good assessment of the performance of the airborne ACDL system.

C. IPDA Theory

The IPDA method was used to retrieve the column concentration of CO_2. In the ACDL system, two lasers with similar wavelengths (defined as λ_{ON} and λ_{OFF}) were emitted, and they were absorbed by CO_2 in the atmosphere. The IPDA double-path differential absorption optical depth (DAOD) can be expressed as

$$\mathrm{DAOD} = \ln \frac{P(\lambda_{\mathrm{off}}) \cdot P_0(\lambda_{\mathrm{on}})}{P(\lambda_{\mathrm{on}}) \cdot P_0(\lambda_{\mathrm{off}})} \tag{1}$$

where P is the power of the echo signal reflected by the ground and P_0 is the power of the emitted laser.

According to the Beer–Lambert law, hydrostatics equation, and ideal gas-state equation, DAOD can be defined as

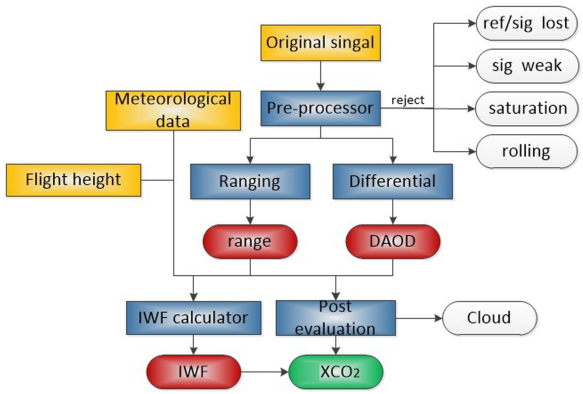

Fig. 2. Schematic of data processing. Yellow backgrounds represent input data. Blue backgrounds represent processing modules. Red backgrounds represent intermediate products. Green background represents the final product. White backgrounds represent different abnormal flags.

where $p_$surface is the ground pressure; $p_$plane is the pressure of airborne platform; σ_{ON} and σ_{OFF} are the absorption cross-sections of CO_2 at λ_{ON} and λ_{OFF}, respectively; xH_2O is the dry-air mixing ratio of H_2O; mH_2O is the average mass of a water-vapor molecule; m_{dryair} is the average mass of dry air; and g is the acceleration due to gravity.

The weighting function (WF) is defined as

$$\mathrm{WF}(p) = \frac{\sigma_{\mathrm{on}}(p) - \sigma_{\mathrm{off}}(p)}{\left(1 + \frac{m_{\mathrm{H_2O}}}{m_{\mathrm{dryair}}} x_{\mathrm{H_2O}}(p)\right) \cdot g \cdot m_{\mathrm{dryair}}}. \tag{3}$$

Then, (2) can be expressed as

$$\mathrm{DAOD} = 2 \int_{p\_\mathrm{surface}}^{p\_\mathrm{plane}} \mathrm{xCO_2}(p) \cdot \mathrm{WF}(p) dp. \tag{4}$$

Finally, the integrated weighting function (IWF) is defined as

$$\mathrm{IWF} = \int_{p\_\mathrm{surface}}^{p\_\mathrm{plane}} \mathrm{WF}(p) dp. \tag{5}$$

The XCO_2 of the entire integrated path from the plane to the surface can be obtained as follows:

$$\mathrm{XCO_2} = \frac{\mathrm{DAOD}}{2\mathrm{IWF}}. \tag{6}$$

D. Inversion Procedures

Fig. 2 shows the schematic of data processing. The data sources mentioned in part *B* of Section II were categorized into three major types, namely, original laser echo signals (abbreviated as original signals), meteorological data, and flight height. The preprocessing module first checked the original signal and rejected specific types of signals. The "lost" flag meant no reference signal was detected. We explain the term "reference signal" in part *B* of Section III. The "lost" flag indicates that the laser transmitter failed to pump a pulse or

$$\mathrm{DAOD} = 2 \int_{p\_\mathrm{surface}}^{p\_\mathrm{plane}} x\mathrm{CO_2}(p) \cdot \frac{\sigma_{\mathrm{on}}(p) - \sigma_{\mathrm{off}}(p)}{\left(1 + \frac{m_{H_2O}}{m_{\mathrm{dryair}}} x_{H_2O}(p)\right) \cdot g \cdot m_{\mathrm{dryair}}} dp \tag{2}$$

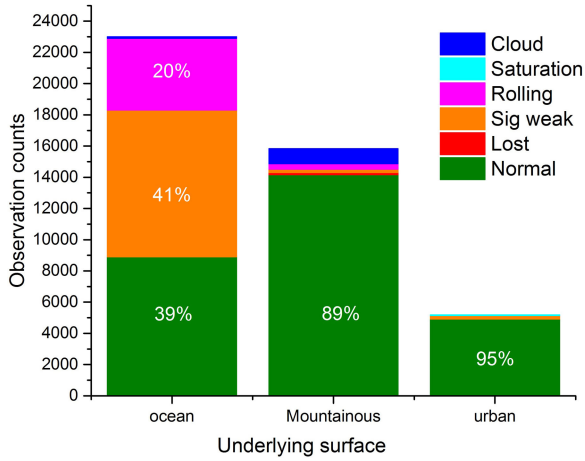

Fig. 3. Proportions of observation pairs with different flags over three underlying surfaces.

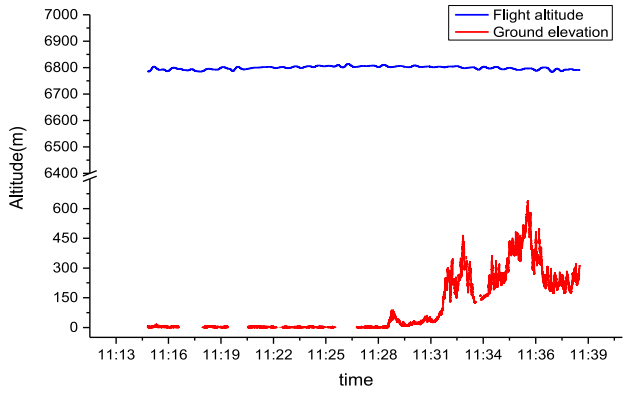

Fig. 4. Flight altitude and ground elevation.

that a pulse was improperly received by detectors. The "sig weak" flag meant that the intensity of received signals failed to exceed 3σ of the background signal. The "saturation" flag indicated that the detectors had a nonlinear response to received signals. Notably, we relied on the echo signal itself to determine whether saturation occurred. Detailed information on how to identify saturation is provided in part B of Section III, wherein we defined original signals. The "rolling" flag indicated that the airplane was rolling. As shown in Fig. 1, in its entire path, the airplane performed three significant turns that were accompanied by rolling. Range information was calculated by applying the laser's time of flight. DAOD was calculated by applying (1), and IWF was calculated using (5). Before calculating XCO_2, another check was performed to identify cloud-reflected cases and unreasonable cases. A major advantage of the IPDA LIDAR over passive remote sensing techniques was its capability to be obtained in the presence of clouds. However, the partial XCO_2 retrieved using reflected signals from clouds still needs to be distinguished from full XCO_2 retrieved with reflected signals from grounds so that users of products can properly utilize these products in their subsequent applications.

III. Results

A. Data Preprocessing

Fig. 3 depicts the proportion of observation pairs with different flags over different underlying surfaces. A total of 66% of observation pairs were labeled as "normal" or "cloud," which meant that the other one-third of observation pairs were excluded from the subsequent inversion procedure. Over land, over 90% of observation pairs passed the preprocessor module. However, only 40% of observation pairs passed the preprocessor module over the ocean. A total of 41% of observation pairs were labeled as "sig weak" over the ocean, resulting in low-efficiency data over the ocean. We believe that the small laser footprint and undulating waves on the ocean were responsible for frequent "sig weak" over the ocean. The laser divergence angle was 0.1 mrad, which was identical to that of the spaceborne version. However, the flight height was 7 km, indicating that the diameter of the footprint of the laser pulse was 0.7 m. Considering that the field of view of the telescope was 1 mrad, echo signals were very easily partially or completely undetectable over the undulating non-Lambertian surface.

The "saturation" flag accounted for only 0.37% of the total observations used in this article. However, such anomalies were commonly encountered throughout the entire series of flight tests. The existence of these anomalies was an important reason why we presented experimental data only for up to 24 min in this article. In the design of this series of flight tests, the performance of the ACDL was expected to be tested under different flight heights. However, the dynamic range of detectors was limited to deal with received signals with high intensity. This problem had already been solved soon after this fight test and is unlikely to arise in future satellite missions because the satellite orbit altitude is constant and the undulating terrain is very small compared with the orbit height of 705 km.

Ground elevation was obtained by subtracting the value of laser ranging from the flight altitude provided by the GPS, as displayed in Fig. 4. It was then compared with the ground elevation provided by Google Earth, and data with large gaps were considered invalid and thus eliminated. Data analysis showed that the invalidity ratio of sea data was high. One possible reason for this situation was that the laser had a smaller divergence angle and the corresponding diameter of the ground footprint was small. When detecting the sea surface, the undulations of waves easily induced specular reflections, causing the echo signal to be out of the telescope's field of view and ultimately resulting in signal loss. In land detection, large continuous data invalidity appeared owing to the apparent inclination of the aircraft during turning. Moreover, the undulating terrain of mountains exerted a great effect on accurate laser ranging. This article focused on the analysis of the detection performance of the airport ACDL system, and continuous CO_2 concentration observation was not the main goal. Therefore, the missing parts of the data were directly eliminated, and only the parts that met the inversion requirements were processed.

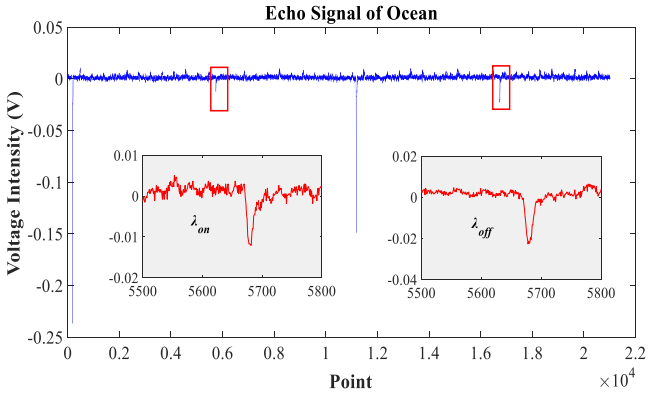

Fig. 5. Echo signals of ocean (total signal and amplification signals of λ_{ON} and λ_{OFF}).

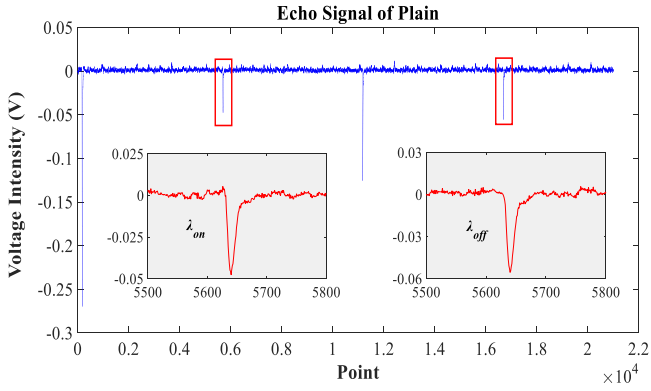

Fig. 6. Echo signals of plain (total signal and amplification signals of λ_{ON} and λ_{OFF}).

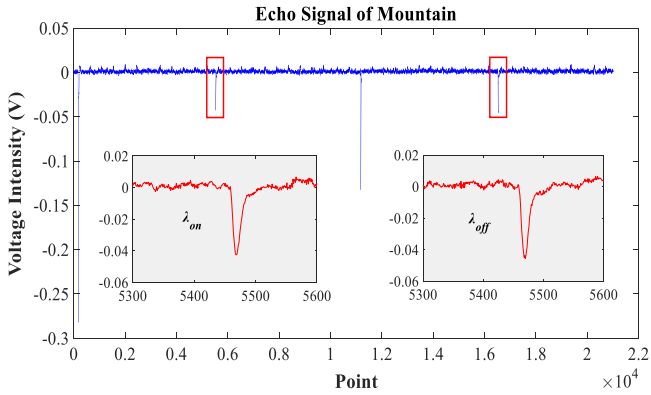

Fig. 7. Echo signals of mountain (total signal and amplification signals of λ_{ON} and λ_{OFF}).

B. Original Echo Signals

As described in this section, we evaluated the performance of the ACDL system by comparing typical echo signals obtained over different surfaces, namely, ocean, urban, and mountainous regions. Furthermore, by showing the echo signal, we further visualized how the preprocessor functioned. Fig. 5 illustrates a typical echo signal obtained over ocean areas. This signal was called as an observation pair, which consisted of four pulses. Starting on the left, the first pulse was the reference signal of the online wavelength. The second pulse was the received signal of the online wavelength. The third and fourth pulses were the reference and received signals of the offline wavelength, respectively. The reference pulses were used to calculate the ratio of the energies of transmitted pulses of different wavelengths. Fig. 5 illustrates explicitly that the energy of an online wavelength pulse was evidently larger than that of an offline pulse. Allocating more energy to the online wavelength pulse at a given total output power helped reduce the random error of the measured DAOD, thereby improving the precision of the retrieved XCO_2 [37].

The most critical parameters we need draw from the original echo signals include the intensity of echo as well as the ranging information. We have tested four indices to estimate the intensity of echo. In the first manner, we fit the laser waveform to the measured signal, and then characterize the intensity of the signal based on this using amplitude and integration. In the second manner, we estimate the signal strength directly using the extreme value or summation. Through pre-experiments, we found that using the parameters obtained by fitting to retrieve XCO_2 can reduce the standard deviation of the inversion results to some extent, but it will cause huge time consumption. Thus, we use the direct method to determine the intensity of signal. After comparing the inversion results of the extreme value method and the summation method, we chose the extreme value method to determine the signal strength because it yielded smaller fluctuations.

According to (4), we need to know p_surface and p_plane to calculate IWF. Both parameters rely on determination of the ranging information. In this article, we utilized ERA5 hourly data on pressure levels to establish a relationship between the atmospheric pressure and the altitude. The elevation of the plane was provided by the onboard GPS equipment. The elevation of the surface is calculated as the plane elevation minus the laser sag distance. We first use the time of flight to determine the distance between the plane and the surface. Then we correct the distance to the vertical elevation difference based on the aircraft pitch and roll angles. Our previous article showed that the accuracy of ranging information was superior 1 m after the implementation of our proposed ranging method [38].

After introducing the data structure of LIDAR echo signals, we further observed the differences among signals obtained over three typical surfaces. Figs. 5–7 illustrate explicitly that the received energy over oceans was much smaller than that received over lands. The corresponding series of echo-signal peaks showed that the pulse on the ocean passed through a slightly longer optical range than that on land. However, such a difference was insufficient to yield significant reductions in received energies. Undoubtedly, the low reflectance of oceans was responsible for the low received energy. No notable differences were observed among the baseline noises shown in the three following figures. Thus, reductions in received energies led to a lower SNR for ocean detections.

Figs. 6 and 7 show small differences between the signals obtained over plain and mountain. In this case, a difference

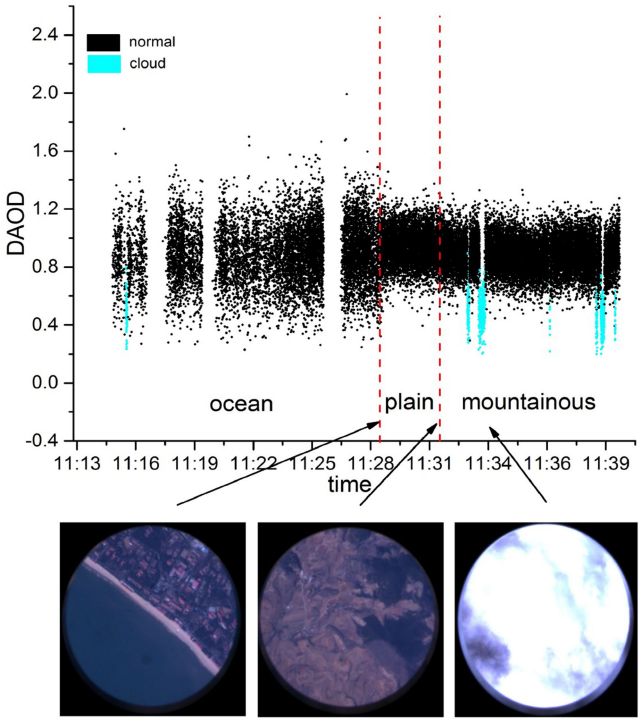

Fig. 8. Measured DAOD during the flight test over different surfaces. The three photographs show the boundary between the ocean and plain areas, the boundary between the plain and mountainous areas, and the cloud.

between the relative random errors (RREs) of retrievals over plain and mountain can be considered independent of SNR.

C. Retrieval Results

Fig. 8 shows the measured DAOD during the flight test. Each measured DAOD was labeled with the corresponding flag assigned by the "post-evaluation" module. Given that the other four conditions in Fig. 3 were already excluded from the differential process, the scatters in Fig. 8 are only in two colors. Moreover, we attached three photographs acquired by the CMOS camera, illustrating three typical scenarios. We divided the surface through which the plane passed into the ocean, plain, and mountainous areas on the basis of GPS information and remotely sensed images provided by Google Earth. Herein, we directly presented photographs acquired during the flight test to validate further such a classification. Additionally, the "post-evaluation" module identified some observations as cloud-reflected samples. We used the time information to find corresponding photographs and verify the validity of the "post-evaluation" module.

In contrast to DAODs over land areas, DAODs over ocean areas exhibited dramatic fluctuations, as shown in Fig. 8. This behavior indicated that the RREs of the measured DAODs were higher over the ocean than over lands. No significant difference was observed in the RREs of DAODs between plains and mountains. This observation was consistent with the inferences presented in part A of Section III.

Fig. 9 illustrates the vertical profiles of pressure, temperature, and humidity obtained by an *in-situ* measuring instrument during

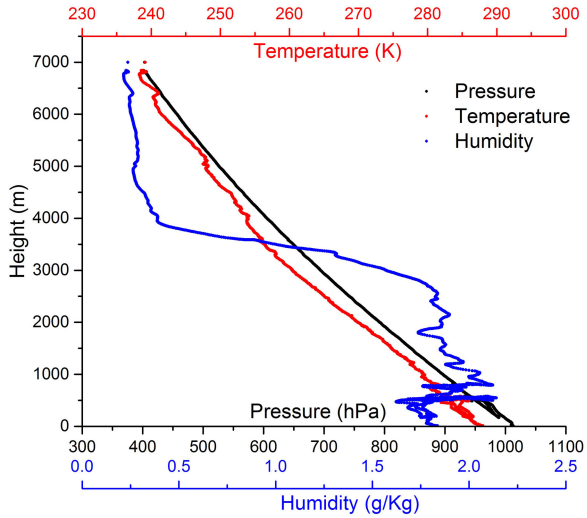

Fig. 9. Vertical profiles of temperature, humidity, and pressure.

landing and takeoff, which were used to calculate IWF. Theoretically, each observation required a corresponding atmospheric profile with respect to its location to calculate IWF. In practice, determining the atmospheric profile at every location was not feasible. A compromise was to utilize the measurements of surface pressure, temperature, and humidity at multiple locations and identical scaling vertical profiles to generate the vertical profiles of atmospheric factors for observations at different locations in a certain area. During the flight test, we performed simultaneous measurements of surface pressure, temperature, and humidity in the study area and found hardly notable differences. Thus, we utilized the vertical profiles of the atmosphere shown in Fig. 9 to calculate IWF for all observations. Notably, we did not measure atmospheric factors over the ocean owing to expenditure limitations. Some errors may have originated from the inaccurate determination of meteorological parameters. Another solution was to use meteorological reanalysis data. However, our study area was excessively small such that it could be completely covered by one or two grids of meteorological reanalysis data. Therefore, even with meteorological reanalysis data, we still set identical atmospheric profiles for all observations.

Fig. 10 shows the IWF for each observation calculated with (5). All variables, except for meteorological data, included the range information extracted by the "ranging" module and the line parameters of CO_2 and H_2O provided by HITRAN2016 [39] and HITEMP2010 [40], respectively. Given the constant elevation of the ocean, IWF was determined primarily by flight height over oceans, thereby exhibiting a very smooth and constant trend. Regardless of whether they acted as uptakes or sources, oceans exhibited highly homogeneous CO_2 fluxes, thereby yielding a constant xCO_2 over oceans in a small extent. Consequently, we assumed that xCO_2 over the route parallel to the coast was constant, providing us a basis to access the precision of retrievals. IWF exhibited smooth changes over the plain area, specifically the urban area. However, IWF fluctuated dramatically over the mountainous area. The mountainous terrain was undulating, which was the main reason for the dramatic fluctuations in

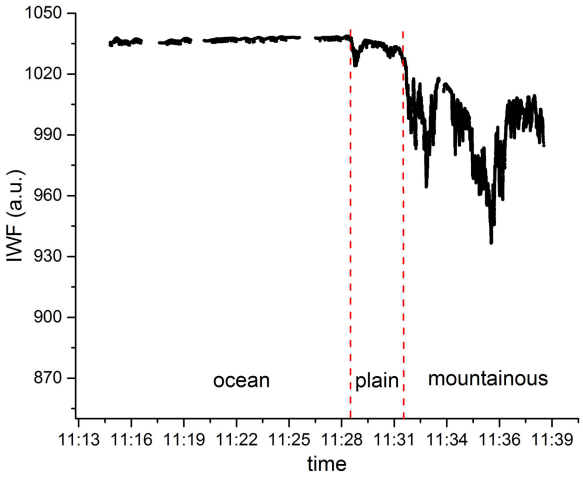

Fig. 10. IWF values calculated by the CO_2 signal of ACDL.

IWF. The accuracy of laser ranging was also degraded in areas with undulating terrain, which further exacerbated the IWF fluctuations.

Fig. 11 shows the XCO_2 retrievals with different settings of integration time. Fig. 11(a) shows that XCO_2 retrievals fluctuated significantly more over the ocean than over land. Fig. 11(b) clearly illustrates the change trend shown by XCO_2 throughout the entire flight track. XCO_2 was the lowest over the ocean area and the highest over the plain area. XCO_2 over mountainous areas was lower than that over plain areas but was higher than that over the ocean. The plain area in this article is an urban area encompassing Qinhuangdao City. A previous article has shown that different estimation methods yielded different estimates of air–sea CO_2 fluxes in the region, but all methods confirmed that the Bohai Sea was a carbon-sink region in winter. Hence, such outcomes as shown in Fig. 11 were reasonable. As described in succeeding sections, we further quantitatively evaluated the results by using the XCO_2 products of OCO-2 and airborne *in-situ* measurements of xCO_2 as references.

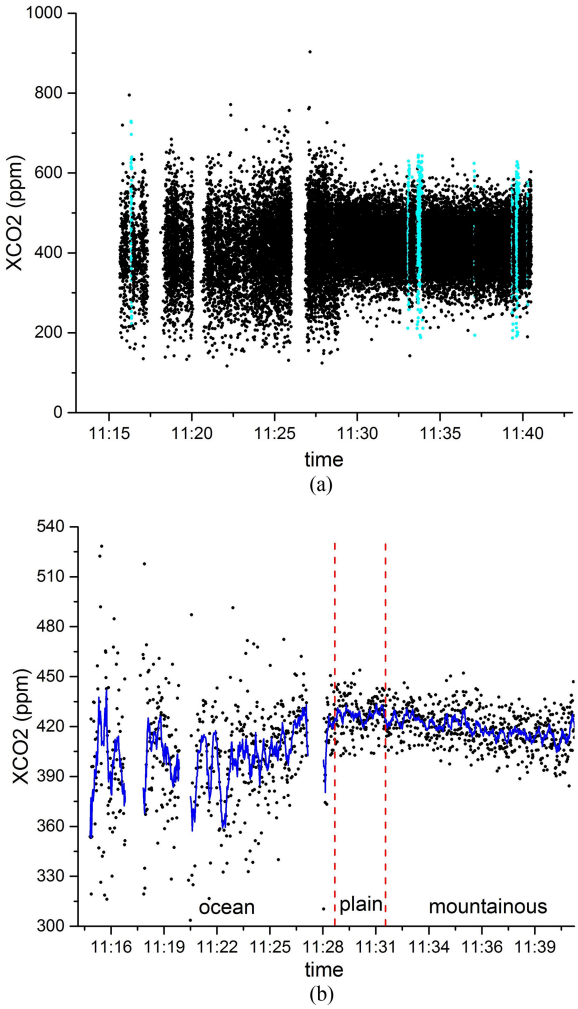

Fig. 11. XCO_2 retrievals. The original per pulse retrievals are shown in Fig. 11(a) with the same legend as that used in Fig. 8. Per-second average retrievals are shown in Fig. 11(b) by black dots, and the 10 s sliding average is shown by the blue line.

D. Performance Evaluation

We needed to obtain the vertical profiles of xCO_2 and further calculate XCO_2 by using the weight function given by (5). Airborne *in-situ* measurements could provide altitude-dependent xCO_2. However, xCO_2 measurements at different altitudes were obtained at different geographical coordinates and times, so they contained spatial and temporal xCO_2 variations. As a compromise, we used three types of indices as references to evaluate the performances of the ACDL. The first one was the standard deviation (STD) of XCO_2 retrievals obtained by the ACDL. Given that XCO_2 can remain constant at a small scale, any variations in XCO_2 can be then regarded as the RRE. STD is a good index for assessing the precision of XCO_2 products acquired by the ACDL. The second one was to calculate an imperfect XCO_2 abusing altitude-dependent xCO_2 obtained through airborne *in-situ* measurements. Although such XCO_2 was never the truth value, it can still serve as a reference. The third index was the XCO_2 products provided by OCO-2. OCO-2 XCO_2 products have been validated and used worldwide [41]–[45]. They can be regarded as a certain standard product of CO_2 concentrations. Comparison with OCO-2 XCO_2 products not only allows us to evaluate the performance of the ACDL products, but also provides insight into the difference between XCO_2 products of sensors with totally different mechanism.

Fig. 12 shows that the STD of retrievals obtained over the ocean was evidently higher than those obtained over lands. STD decreased with increased integration time for all three underlying surfaces. The actual STD curves did not coincide with the ideal curves, especially for the ocean case, indicating that some bias may exist in retrievals over the ocean. The mean STDs of 1.93, 0.85, and 0.96 ppm were obtained for the ocean, plain, and mountainous areas, respectively. The mean XCO_2 values were 411.07, 425.71, and 417.87 ppm for the ocean, plain, and mountainous areas, respectively, with RRE values of 0.47%, 0.20%, and 0.23%, respectively. The random error of XCO_2 retrievals was significantly higher over the ocean than over land. ACDL exhibited optimum performance over the plain and then

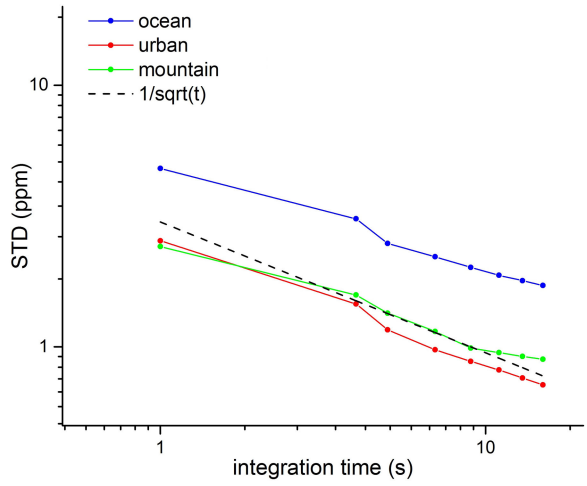

Fig. 12. Relationship between STD and the integration time. Blue, red, and green dots represent results obtained over ocean, plain, and mountainous area. Solid lines represent actual STD, whereas dotted lines represent the $1/\sqrt{t}$ which is added for comparison.

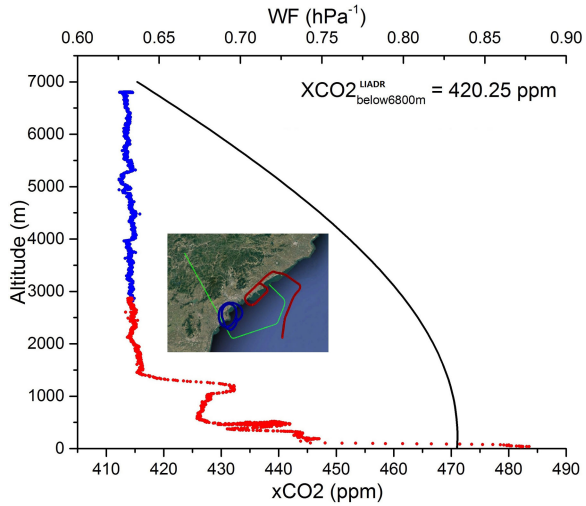

Fig. 13. XCO_2 below 6800 m calculated using measured xCO_2 profiles. The black line represents the WF. Colorful dots represent the measured xCO_2 vertical profile. The picture in the figure shows where the altitude-dependent xCO_2 was obtained.

over the mountainous area. We believe that the low SNR of echo signals obtained over the ocean led to the worst performance of ACDL over the ocean. As shown by Figs. 6–8, the echo signals and the measured DAOD of the plain and mountainous areas lacked evident differences. The difference in the STD could be attributed to the precision of the range information. Large slopes and terrain undulations are extensively considered to be factors that degrade the accuracy of laser ranging. Overall, the XCO_2 retrievals were stable after 10 s of averaging, and the random error was less than 1 ppm in the terrestrial region.

We also attempted to calculate XCO_2 by using the measured xCO_2 profiles, as shown in Fig. 13. On March 14, the aircraft performed gyroscopic flight to obtain vertical CO_2 distribution. The gyroscopic track is illustrated in blue, and its corresponding xCO_2 measurements are also shown in blue dots in Fig. 13.

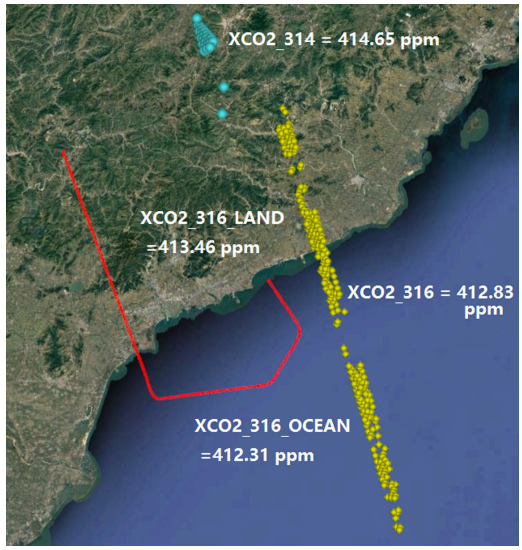

Fig. 14. XCO_2 products provided by OCO-2. Blue dots represent the spatial distributions of XCO_2 products obtained on March 14, 2019, whereas yellow dots represent those obtained on March 16, 2019.

Unfortunately, the plane descended from approximately 6800 to 2000 m but not to the ground during gyroscopic flight. On March 14, xCO_2 recording was stopped at nearly half an hour before landing. To obtain the vertical profiles of xCO_2 below 2000 m, we searched for xCO_2 measurements taken during an adjacent flight test on March 9. On that day, xCO_2 profiles were fully recorded during the landing process, when the plane descended from 2900 m to the ground. We corrected for the difference between the 2 days by using data from 2900 to 2000 m to obtain a corrected value for the xCO_2 of March 9. Notably, the vertical profile of xCO_2 was obtained in 2 days and in two regions. Therefore, inevitable biases from the truth value existed. XCO_2 was calculated as 420.25 ppm by using the vertical profile of xCO_2 and the altitude-dependent WF shown in Fig. 13. We noticed that the most dramatic changes in the vertical profile of xCO_2 occurred below 1500 m. The plane collected this part of the data off the coast. In this flight, the plane crossed the boundary of the ocean and the plain at 11:28:42. Thus, we calculated the average of XCO_2 from 11:28:12 to 11:29:12 when the plane crossed from the ocean to the urban area. The resultant XCO_2 was 419.31 ppm, which was very close to 420.25 ppm. Therefore, the ACDL exhibited good sensitivity for reflecting variation in xCO_2 and a strong capability to obtain XCO_2 with a high accuracy.

We searched the OCO-2 product dataset in the study area for the 3 days around March 14, 2019 and found that XCO_2 products for March 14 and 16, 2019 were available. Fig. 14 shows that the XCO_2 observations obtained by OCO-2 on March 16 were closer to those obtained for the study area and were higher in quantity. On March 16, the XCO_2 of OCO-2 fluctuated between 401.4 and 420.6 ppm, with an average value of 412.83 ppm. On March 14, the XCO_2 of OCO-2 fluctuated between 410.8 and 420.0 ppm, with an average value of 414.65 ppm. The XCO_2 retrievals of OCO-2 also suggested the existence of an xCO_2 gradient between the ocean and land despite being lower

than the results of the ACDL. It is also witnessed that there is an evident difference between the XCO_2 of ACDL and the XCO_2 of OCO-2. The mean XCO_2 of ACDL was 416.26 ppm, whereas the mean XCO_2 of OCO-2 on March 14 and 16 were 414.65 and 412.83 ppm, respectively. These differences could be attributed to the following reasons. First, in contrast to that of the airborne IPDA LIDAR pathway, the XCO_2 product of OCO-2 did not cover urban areas. xCO_2 in the urban area is extensively thought to be higher than that in suburban areas, which is the so-called urban CO_2 dome [46]. Second, XCO_2 in this article was actually partial XCO_2. Considering that xCO_2 in the lower troposphere was significantly higher than that in high-altitude regions, partial XCO_2 was evidently higher than full XCO_2. Finally, systematic errors originating from the instrument itself may also be a cause. We also used the vertical profile of xCO_2 shown in Fig. 13 to calculate XCO_2 of OCO-2 and full XCO_2 of ACDL, setting xCO_2 as 413 ppm above 6800 m. The resultant truth full XCO_2 were 416.96 and 418.43 ppm for OCO-2 and ACDL, respectively. Considering the distance between the inner mountainous area and the coastline, a difference of 2.31 ppm was reasonable. Meanwhile, full XCO_2 of ACDL was larger, exhibiting a stronger ability to reflect the underlying surface CO_2 fluxes.

Moreover, there is a very complicated problem arising in comparisons of LIDAR-derived and spectrometers-derived XCO_2. As we know, current retrieval algorithms of OCO-2/3, GOSAT-1/2, TanSat and other similar sensors all use averaging kernels to calculate the final XCO_2 products. However, dual-wavelength IPDA LIDARs do no yield an averaging kernel but directly calculate the column-weighted xCO_2. Therefore, it is questionable to directly compare two products. This would be an urgent concern when we need to validate XCO_2 products of the forthcoming ACDL using current remotely sensed XCO_2 products.

IV. Discussion

A. Implications for the Future Space-Borne Mission

One of the most important aims of the flight was is to set a reference for the forthcoming space-borne mission. Although performance evaluations were conducted a few years ago, the flight test provided us with a unique opportunity to compare simulated results with real measurements, which was crucial for the projection of the performance of the space-borne mission. As described in this subsection, we utilized the performance-evaluation model, which was introduced in detail in our previous publications, to simulate the RRE by using the remotely sensed products of surface reflectance and aerosol optical depth as variables. The configuration of space-borne CO_2-IPDA LIDAR can be found in our previous articles [16], [27], [47] and that of the airborne prototype can be found in a recent publication by Zhu *et al.* [48].

Fig. 15 illustrates the outcomes of the performance evaluation model for two configurations. Comparing RREs under identical spatial and temporal scales was unwise considering the different repetition frequencies and velocities of platforms. Instead, we directly showed the RREs of a single observation pair, i.e., an observation of online wavelength plus an observation of offline wavelength such that RREs with a specific spatial or temporal scale could be further easily estimated by through simple mathematical operations [49].

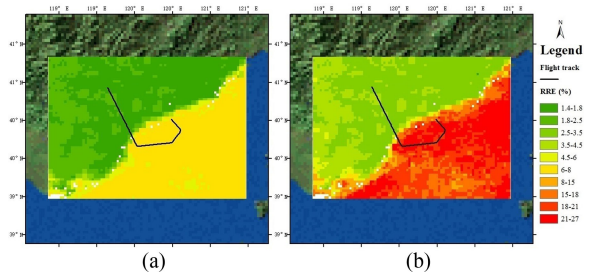

Fig. 15. Simulated spatial distribution of the RRE of a single observation pair by using an identical performance-evaluation model but different configurations: (a) shows the results for the airborne prototype, and (b) shows the results for the space-borne one.

Fig. 15(a) shows that the RRE of a single observation pair was approximately 6%–8% over seas and approximately 2.5%–3.5% over lands. Given that the repetition frequency of the airborne prototype was 30 Hz, it takes a time integration of ∼4 and 13 s to achieve an RRE of less than 0.3% for lands and seas, respectively. Comparison with the results obtained with a 10 s sliding averaging revealed that the real errors were consistent with the simulated ones. For example, the RRE theoretically dropped to 0.15% for lands, i.e., about 0.63 ppm, after a 10 s sliding averaging, whereas the actual result was 0.75 ppm. For oceans, the theoretical random error was 1.39 ppm after a 10 s sliding averaging, and the actual value was 1.35 ppm. We believe the reflectance could be underestimated, resulting in overestimated RRE over the ocean. Normally, the theoretical RRE was slightly lower than the actual one because the performance-evaluation model ignored some factors that influenced the RRE more or less. Therefore, the performance-evaluation model was capable of providing very useful guidance for the satellite mission.

From Fig. 15(b), we concluded that obtaining XCO_2 with an RRE less than 1 ppm over oceans at a spatial resolution of 100 km was challenging or even impossible. Our previous work has already indicted that inshore coastal waters would be the area with the worst detection results because of their low reflectance and high AOD. In our previous article, we set the reflectance of seas as 0.05. In the current one, we obtained the surface reflectance by using the MODIS (Terra/Aqua) 5 km and 16 day composite bidirectional reflectance distribution function-adjusted data at band 6 (1.64 μm). Considering that the sea in our study area belongs to inshore coastal waters, the surface-reflectance product provided valid values. We noticed that the mean reflectance over the sea in our study area was about 0.014, which was much smaller than 0.05. Hence, the RRE in this article was even higher than before. Fig. 14 also highlights the significance of using a performance-evaluation model. The mapping of the RRE of airborne detection to that of space-borne detection cannot be a simple linear stretch. Fig. 15(a) and the results presented in previous sections demonstrated that the RRE of a single observation pair over oceans was approximately twice of that over lands for the airborne test. However, for the

space-borne detection, the RRE over lands was four to five times of that over waters. Considering that the preset spatial resolution of XCO_2 products over oceans was only twice of that over lands, which was equivalent to a 1.4-fold reduction in RRE, we did not think that RREs of less than 1 ppm could be obtained over oceans for the forthcoming mission, unless some dedicated retrieval algorithms for observations obtained over oceans are developed. The good news is that the RRE of XCO_2 products over lands was expected to be less than 1 ppm for the forthcoming space-borne CO_2-IPDA LIDAR if the designed configuration would be fully realized.

B. Other Issues Revealed by the Flight Campaign

Although the main goal of the flight campaign was to test the prototype of space-borne CO_2-IPDA LIDAR from a technical perspective, its results also provided insights into the characteristics of xCO_2 distribution caused by carbon sinks and sources. A strong xCO_2 enhancement owing to anthropogenic carbon emissions was observed in this article. Although Qinhuangdao is only a medium-sized city in China, its urban CO_2 dome can be explicitly measured by the airborne IPDA LIDAR.

Moreover, this experiment provided indirect evidence that the winter ocean is a carbon sink. The mean XCO_2 over the ocean was 411.07 ppm. Fig. 13 shows that xCO_2 was approximately 414 ppm at high altitudes, indicating that xCO_2 was less than 411 ppm near the ocean surface. These results indicated that the ocean served as an atmospheric CO_2 sink at least during winter.

The vertical profile of xCO_2, a by-product of this flight campaign, showed that the vertical gradient of xCO_2 was considerably more distinct than the horizontal gradient of a column averaged/weighted xCO_2. Some novel means to measure the vertical gradients of xCO_2 in the lower troposphere can considerably help us infer the anthropogenic carbon emissions or natural carbon sinks.

We also found that the XCO_2 obtained by IPDA-LIDAR was highly sensitive to xCO_2 variations in the lower troposphere. Notably, a gradient of 15 ppm was measured between the ocean and the urban area, thereby laying a good foundation for the further inversion of CO_2 fluxes. Furthermore, the IPDA-LIDAR also exhibited good performances over mountainous areas.

At the same time, the experiment also exposed some problems, which were exactly what the developer team of the ACDL should strive for in the future. First, we lack effective means for validating the XCO_2 products of IPDA LIDAR. As shown in Fig. 13, the partial XCO_2-LIDAR was calculated to be 420.25 ppm. We also calculated the partial XCO_2 of OCO-2 using the same vertical profile of xCO_2 and the outcome was 419.86 ppm. Current TCCON sites may not provide a suitable benchmark for the validation of a space-borne IPDA LIDAR. Accordingly, we needed the vertical profiles of xCO_2, especially in the lower troposphere, to validate the products of IPDA LIDAR but not those of XCO_2. Second, a large proportion of observation pairs were excluded from the subsequent inversion procedure. In this article, a total of only nearly 30 min of data was needed for the experiments because other data did not pass the data-quality check. Among anomalous flags, the "rolling" flag is inevitable for airborne tests but will not occur in the future space-borne mission. The "saturation" flag is also unlikely to occur in the space-borne mission but should be avoided in the next flight tests. The "sig weak" flag is the focus of the next phase of article. In the current article, 41% of observation pairs were labeled as "sig weak" over the ocean. In other datasets, the proportion was even larger. Third, the prospect of XCO_2 detections over oceans is pessimistic. A large gap exists between the state-of-the-art technique of LIDAR and the desired goal, i.e., obtaining XCO_2 with RRE less than 1 ppm at a spatial resolution of 100 km over oceans. Hence, we urge the development of dedicated inversion algorithm for XCO_2 detection over oceans.

V. Conclusion

We analyzed the data obtained with an airborne CO_2-IPDA LIDAR to evaluate the performance of the forthcoming Atmospheric Environment Monitoring Satellite of China and to determine the characteristics of xCO_2 distribution by determining anthropogenic emissions and natural uptakes. An initial version of the data-processing frameworks was developed to assess the validity of the observations acquired by the IPDA LIDAR automatically and to further obtain XCO_2 retrievals. We successfully acquired valid XCO_2 retrievals over urban, ocean, and mountainous areas and clouds. The mean XCO_2 values obtained for the ocean, urban, and mountainous areas with a 10 s sliding average were 411.07, 425.71, and 417.87 ppm with STDs of 1.93, 0.85, and 0.96 ppm, respectively. The change trend of XCO_2 coincided well with those of xCO_2 measurements obtained by *in-situ* equipment during flight at approximately 6800 m. A vertical profile of xCO_2 was obtained using a spiral descent track and landing track, yielding a pseudo-*in-situ* XCO_2 measurement that could be used for comparison with LIDAR-based XCO_2. The difference between the two values was only 0.76 ppm. Moreover, the XCO_2 products of OCO-2 confirmed the existence of the ocean–land gradient of CO_2 concentrations. We found that the difference between XCO_2 truths of OCO-2 and ACDL based on the same vertical profile of xCO_2 was nearly 1.5 ppm, suggesting that XCO_2 of LIDAR was more capable of revealing the characteristics of surface CO_2 fluxes because of its WF.

This result also proved that validating the products of space-borne IPDA LIDAR by using ground-based FTIR is unwise. Regarding the scientific significance, we found that the intensity of CO_2 anomalies caused by the urban CO_2 dome exceeded 8 ppm. The CO_2 gradient for an urban area near an ocean could even be as high as 15 ppm, indicating strong CO_2 uptake by the ocean. Considerable work has to be performed on the development of novel algorithms and improvements in hardware systems before satellite launching to further enhance the performance of the onboard CO_2-IPDA LIDAR. We look forward to unprecedented CO_2-concentration observations obtained using the space-borne LIDAR, which promises to provide us with a unique opportunity to look into the carbon cycle.

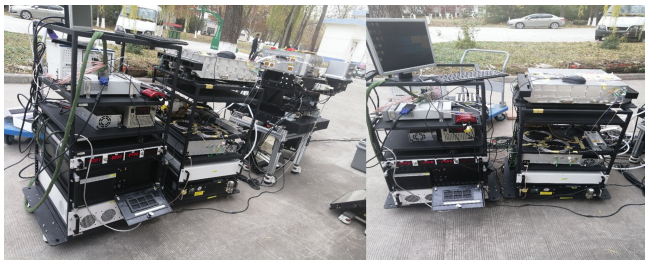

Fig. 16. Photographs of the airborne ACDL system.

TABLE I
PRIMARY PARAMETERS OF THE ACDL SYSTEM

Category	Parameters	Value
Laser transmitter	Wavelength	1572.024 nm@online 1572.085 nm@offline
	Pulse energy(on/off)	6 mJ
	Pulse width(on/off)	17 ns
	Repetition rate	30 Hz
	Frequency stability	2.7 MHz
	Linewidth	50 MHz
	Beam divergence	0.6 mrad
	Pulse spectral width (OPA)	30 MHz
	Emission optical efficiency	0.8955
Receiver	Telescope diameter	150 mm
	Field of view	1.0 mrad
	Receiver optical efficiency	0.3797
	Responsivity	0.94 A/W
	NEP	64 fW/$\sqrt{Hz}$
	Excess noise factor	3.2
	Data acquisition	125 MS/s
	Optical filter bandwidth	0.45 nm

APPENDIX
INTRODUCTION TO ACDL SYSTEM

The photographs of the ACDL system are shown in Fig. 16, and its primary parameters are listed in Table I.

The ACDL system is composed of optical transceiver system, acquisition system, temperature control system, electronic control equipment, seed laser, and frequency stabilization system. The optical transceiver system consists of a pulse laser, a telescope, a receiving optical system, and an APD detector, which is installed in a pod outside the aircraft. The INS is mounted on the same pedestal as the pulsed laser emitter, with markings pointing in the same direction as the forward direction of the aircraft. The time, altitude, and attitude information obtained by INS and GPS are marked in front of the lidar signal every 0.05 s.

The seed laser can generate two stable wavelengths (1572.024 and 1572.085 nm) as online and offline seed lasers, respectively. The fiber-optical beam splitter (FOS) divides the seed laser into two parts. One part is injected into the OPO cavity, and the other part laser frequency is shifted by 400 MHz from the acousto-optic modulator (AOM) to reduce the overlap between the intensity envelope of the optical pulse and the beat signal of the optical heterodyne. The two beams of light output from the OPO cavity and AOM are synthesized by FOS and then heterodyne beat frequency. In the frequency stabilization system, the OPO laser is controlled by feedback from a photodetector detecting the frequency value of the beat signal to obtain a 1572 nm pulsed laser with stable frequency.

The acquisition system, temperature control system, electronic control equipment, seed laser, and frequency stabilization system are installed inside the aircraft, and the information is transmitted to the transceiver system in the pod through optical fibers and cables protected by armor sleeves. The temperature control subsystem monitors and regulates the temperature of the cooling water tank and the thermal control box to keep the instruments in the pod at the normal working temperature. As the nerve center of the laser transmitter, the electronic control system is controlled by the upper computer software, provides secondary power supply, and controls the timing of laser output and the start timing of the laser transmitter. It also provides power distribution for InGaAs APD detectors and many other instruments. The acquisition card converts the analog signal of the APD detector into digital signal, which is collected and stored by computer. The computer also works with corresponding software to collect and store information about INS, GPS, online laser frequency, temperature, humidity, and pressure.

REFERENCES

[1] T. Stocker *et al.*, *IPCC, 2013: Climate Change 2013: The Physical Science Basis. Contribution of Working Group I to the Fifth Assessment Report of the Intergovernmental Panel on Climate Change*. Cambridge, U.K.: Cambridge Univ. Press, 2014.

[2] B. B. Stephens *et al.*, "Weak northern and strong tropical land carbon uptake from vertical profiles of atmospheric CO_2," *Science*, vol. 316, no. 5832, pp. 1732–1735, 2007.

[3] A. J. Watson *et al.*, "Tracking the variable North Atlantic Sink for atmospheric CO_2," *Science*, vol. 326, no. 5958, pp. 1391–1393, 2009.

[4] P. E. Dennison *et al.*, "High spatial resolution mapping of elevated atmospheric carbon dioxide using airborne imaging spectroscopy: Radiative transfer modeling and power plant plume detection," *Remote Sens. Environ.*, vol. 139, pp. 116–129, 2013.

[5] P. J. Rayner and D. M. O'Brien, "The utility of remotely sensed CO_2 concentration data in surface source inversions," *Geophys. Res. Lett.*, vol. 28, no. 1, pp. 175–178, 2001.

[6] F. M. Schwandner *et al.*, "Spaceborne detection of localized carbon dioxide sources," *Science*, vol. 358, no. 6360, 2017, Art. no. 192.

[7] A. Liang, G. Wei, H. Ge, and X. Chengzhi, "Comparison of satellite-observed XCO_2 from GOSAT, OCO-2, and ground-based TCCON," *Remote Sens.*, vol. 9, no. 10, 2017, Art. no. 1033.

[8] M. Buchwitz *et al.*, "Global satellite observations of column-averaged carbon dioxide and methane: The GHG-CCI XCO_2 and XCH_4 CRDP3 data set," *Remote Sens. Environ.*, vol. 203, pp. 276–295, 2017.

[9] A. Bril, S. Oshchepkov, and T. Yokota, "Application of a probability density function-based atmospheric light-scattering correction to carbon dioxide retrievals from GOSAT over-sea observations," *Remote Sens. Environ.*, vol. 117, pp. 301–306, 2012.

[10] X. Chen *et al.*, "Angular dependence of aerosol information content in CAPI/TanSat observation over land: Effect of polarization and synergy with A-train satellites," *Remote Sens. Environ.*, vol. 196, pp. 163–177, 2017.

[11] A. Chatterjee *et al.*, "Influence of el Nino on atmospheric CO_2 over the tropical Pacific Ocean: Findings from NASA's OCO-2 mission," *Science*, vol. 358, no. 6360, 2017, Art. no. 190.

[12] A. Eldering *et al.*, "The orbiting carbon observatory-2 early science investigations of regional carbon dioxide fluxes," *Science*, vol. 358, no. 6360, 2017, Art. no. 188.

[13] Y. Sun *et al.*, "OCO-2 advances photosynthesis observation from space via solar-induced chlorophyll fluorescence," *Science*, vol. 358, no. 6360, 2017, Art. no. 189.

[14] J. Xiao *et al.*, "Remote sensing of the terrestrial carbon cycle: A review of advances over 50 years," *Remote Sens. Environ.*, vol. 233, 2019, Art. no. 111383.

[15] J. B. Abshire *et al.*, "Pulsed airborne lidar measurements of atmospheric CO_2 column absorption," *Tellus B*, vol. 62, no. 5, pp. 770–783, 2010.
[16] G. Han *et al.*, "Performance evaluation for China's planned CO_2-IPDA," *Remote Sens.*, vol. 9, no. 8, 2017, Art. no. 768.
[17] H. Boesch, D. Baker, B. Connor, D. Crisp, and C. Miller, "Global characterization of CO_2 column retrievals from shortwave-infrared satellite observations of the orbiting carbon observatory-2 mission," *Remote Sens.*, vol. 3, no. 2, pp. 270–304, 2011.
[18] R. V. Martin, "Satellite remote sensing of surface air quality [J]," *Atmos. Environ.*, vol. 42, no. 34, pp. 7823–7843, 2008.
[19] J. B. Abshire, A. Ramanathan, H. Riris, G. R. Allan, and J. Digangi, "Airborne measurements of CO_2 column concentrations made with a pulsed IPDA lidar using a multiple-wavelength-locked laser and HGCDTE APD detector," *Atmosp. Meas. Techn.*, vol. 11, no. 4, pp. 1–36, 2017.
[20] Y. Zhu, J. Liu, X. Chen, X. Zhu, D. Bi, and W. Chen, "Sensitivity analysis and correction algorithms for atmospheric CO_2 measurements with 1.57-um airborne double-pulse IPDA LIDAR," *Opt. Exp.*, vol. 27, no. 22, pp. 32679–32699, 2019.
[21] J. Du *et al.*, "Double-pulse 1.57 um integrated path differential absorption lidar ground validation for atmospheric carbon dioxide measurement," *Appl. Opt.*, vol. 56, no. 25, pp. 7053–7058, 2017.
[22] T. F. Refaat, U. N. Singh, J. Yu, M. Petros, R. Remus, and S. Ismail, "Double-pulse 2-μm integrated path differential absorption lidar airborne validation for atmospheric carbon dioxide measurement," *Appl. Opt.*, vol. 55, no. 15, pp. 4232–4246, 2016.
[23] U. N. Singh, J. Yu, M. Petros, T. Refaat, and K. Reithmaier, "Development of a pulsed 2-micron integrated path differential absorption lidar for CO_2 measurement," *Lidar Remote Sens. Environ. Monit. XIV*, vol. 8872, 2013, Art. no. 887209.
[24] J. Caron, Y. Durand, J. L. Bezy, and R. Meynart, "Performance modeling for A-SCOPE: A space-borne lidar measuring atmospheric CO_2," in *Proc. SPIE Eur. Remote Sens.*, 2009, Art. no. 74790E.
[25] A. Amediek, A. Fix, G. Ehret, J. Caron, and Y. Durand, "Airborne lidar reflectance measurements at 1.57 μm in support of the A-SCOPE mission for atmospheric CO_2," *Atmos. Meas. Techn.*, vol. 2, no. 3, pp. 755–772, 2009.
[26] B. Lin *et al.*, "Atmospheric CO_2 column measurements in cloudy conditions using intensity-modulated continuous-wave lidar at 1.57 micron," *Opt. Exp.*, vol. 23, no. 11, pp. 582–593, 2015.
[27] G. Han *et al.*, "Feasibility study on measuring atmospheric CO_2 in urban areas using spaceborne CO_2-IPDA LIDAR," *Remote Sens.*, vol. 10, no. 7, 2018, Art. no. 985.
[28] C. Kiemle, G. Ehret, A. Amediek, A. Fix, M. Quatrevalet, and M. Wirth, "Potential of spaceborne lidar measurements of carbon dioxide and methane emissions from strong point sources," *Remote Sens.*, vol. 9, no. 11, 2017, Art. no. 1137.
[29] S. Kawa, J. Mao, J. Abshire, G. Collatz, X. Sun, and C. Weaver, "Simulation studies for a space-based CO_2 lidar mission," *Tellus B*, vol. 62, no. 5, pp. 759–769, 2010.
[30] X. Zhang *et al.*, "The development and application of satellite remote sensing for atmospheric compositions in China," *Atmos. Res.*, vol. 245, 2020, Art. no. 105056.
[31] A. Amediek *et al.*, "CHARM-F-a new airborne integrated-path differential-absorption lidar for carbon dioxide and methane observations: Measurement performance and quantification of strong point source emissions," *Appl. Opt.*, vol. 56, no. 18, pp. 5182–5197, 2017.
[32] J. Mao *et al.*, "Measurement of atmospheric CO_2 column concentrations to cloud tops with a pulsed multi-wavelength airborne lidar," *Atmos. Meas. Techn.*, vol. 11, no. 1, pp. 1–26, 2018.
[33] L. Labzovskii, S. Jeong, and N. C. Parazoo, "Working towards confident spaceborne monitoring of carbon emissions from cities using orbiting carbon observatory-2," *Remote Sens. Environ.*, vol. 233, 2019, Art. no. 111359.
[34] A. Eldering *et al.*, "The orbiting carbon observatory-2: First 18 months of science data products," *Atmos. Meas. Techn.*, vol. 10, no. 2, pp. 549–563, 2016.
[35] H. Boesch, D. F. Baker, B. J. Connor, D. Crisp, and C. E. Miller, "Global characterization of CO_2 column retrievals from shortwave-infrared satellite observations of the orbiting carbon observatory-2 mission," *Remote Sens.*, vol. 3, no. 2, pp. 270–304, 2011.
[36] C. Frankenberg *et al.*, "Prospects for chlorophyll fluorescence remote sensing from the orbiting carbon observatory-2," *Remote Sens. Environ.*, vol. 147, pp. 1–12, 2014.
[37] J. Caron and Y. Durand, "Operating wavelengths optimization for a spaceborne lidar measuring atmospheric CO_2," *Appl. Opt.*, vol. 48, no. 28, pp. 5413–5422, 2009.
[38] X. Ma, H. Zhang, G. Han, H. Xu, and S. Li, "High-precision CO_2 column length analysis on the basis of a 1.57-μm dual-wavelength IPDA Lidar," *Sensors*, vol. 20, no. 20, 2020, Art. no. 5887.
[39] C. Hill, I. E. Gordon, R. V. Kochanov, L. Barrett, J. S. Wilzewski, and L. S. Rothman, "HITRANonline: An online interface and the flexible representation of spectroscopic data in the HITRAN database," *J. Quant. Spectrosc. Radiative Transf.*, vol. 177, pp. 4–14, 2016.
[40] L. Rothman *et al.*, "HITEMP, the high-temperature molecular spectroscopic database," *J. Quant. Spectrosc. Radiative Transf.*, vol. 111, no. 15, pp. 2139–2150, 2010.
[41] A. Liang, G. Han, W. Gong, J. Yang, and C. Xiang, "Comparison of global XCO_2 concentrations from OCO-2 with TCCON data in terms of latitude zones," *IEEE J. Sel. Topics Appl. Earth Observ. Remote Sens.*, vol. 10, no. 6, pp. 2491–2498, Jun. 2017.
[42] R. Qiu *et al.*, "CO_2 concentration, a critical factor influencing the relationship between solar-induced chlorophyll fluorescence and gross primary productivity," *Remote Sens.*, vol. 12, no. 9, 2020, Art. no. 1377.
[43] D. Wunch *et al.*, "Comparisons of the orbiting carbon observatory-2 (OCO-2) XCO_2 measurements with TCCON," [Discussion paper], 2016.
[44] J. Hakkarainen, I. Ialongo, and J. Tamminen, "Direct space-based observations of anthropogenic CO_2 emission areas from OCO-2," *Geophys. Res. Lett.*, vol. 43, no. 21, pp. 11400–11406, 2016.
[45] S. M. R. Crowell *et al.*, "On the ability of space-based passive and active remote sensing observations of CO_2 to detect flux perturbations to the carbon cycle," *J. Geophys. Res. Atmos.*, vol. 123, no. 2, pp. 1460–1477, Jan. 2018.
[46] K. George, L. H. Ziska, J. A. Bunce, and B. Quebedeaux, "Elevated atmospheric CO_2 concentration and temperature across an urban-rural transect," *Atmos. Environ.*, vol. 41, no. 35, pp. 7654–7665, 2007.
[47] T. Shi *et al.*, "Quantifying CO_2 uptakes over oceans using LIDAR: A tentative experiment in Bohai Bay," *Geophys. Res. Lett.*, vol. 48, no. 9, pp. 1–8, May 2021.
[48] Y. Zhu, J. Yang, X. Chen, X. Zhu, and W. Chen, "Airborne validation experiment of 1.57-μm double-pulse IPDA LIDAR for atmospheric carbon dioxide measurement," *Remote Sens.*, vol. 12, no. 12, 2020, Art. no. 1999.
[49] G. Ehret, R. Kiemle, R. Wirth, R. Amediek, R. Fix, and R. Houweling, "Space-borne remote sensing of CO_2, CH_4, and N_2O by integrated path differential absorption lidar: A sensitivity analysis," *Appl. Phys.*, vol. B90, no. 3/4, pp. 593–608, 2008.

Chengzhi Xiang received the Ph.D. degree in photogrammetry and remote sensing from Wuhan University, Wuhan, China, in 2017.

He is currently working with the School of Remote Sensing and Geomatics Engineering, Nanjing University of Information Science and Technology, Nanjing, China. His research interests include LIDAR, remote sensing of ecological environment, carbon cycle, etc.

Xin Ma received the B.S., M.S. degree in engineering of surveying and mapping, and Ph.D. degree photogrammetry and remote sensing from Wuhan University, Wuhan, China, in 2010, 2013, and 2016, respectively.

He is an Assistant Professor with the State Key Laboratory of Information Engineering in Surveying, Mapping and Remote Sensing, Wuhan University. His research interests include LIDAR and atmospheric remote sensing.

Xingying Zhang received the B.S. degree in material science and engineering from Beijing University of Aeronautics and Astronautics, Beijing, China, in 2001, and the Ph.D. degree in atmospheric chemistry from Beijing Normal University, Beijing, in 2006.

He is currently a Deputy Director with the National Satellite Meteorological Center, China Meteorological Administration. He has authored/coauthored more than 120 research articles in science journals and books. His research interests include satellite observation and *in-situ* measurement of atmospheric components and its applications to climate and environmental problems.

Ge Han received the B.S. and M.S. degrees in geodetection and information technology from the China University of Geosciences, Wuhan, China, in 2009 and 2012, respectively, and the Ph.D. degree in remote sensing from the State Key Laboratory of Information Engineering in Surveying, Mapping and Remote Sensing, Wuhan University, Wuhan, China, in 2015.

He is currently an Associate Professor with the School of Remote Sensing and Information Engineering, Wuhan University. His research interests include remote sensing of greenhouse gases and LIDAR.

Binglong Chen received the Ph.D. degree in optical engineering from the Beijing Institute of Technology, Beijing, China, in 2016.

He is currently an Assistant Researcher with the National Satellite and Meteorological Center, China Meteorological Administration, Beijing. His research interests include data processing method in aerosol and atmospheric temperature detected LIDAR.

Wanchun Zhang received the B.S. degree in information science from China Agriculture University, Beijing, China, in 2008, and the M.S. and Ph.D. degrees in cartography and geographic information systems from Aerospace Information Research Institute, Chinese Academy of Sciences, Beijing, in 2012 and 2015, respectively.

She is currently an Associate Researcher with the National Satellite Meteorological Center of China Meteorological Administration. Her research interests include satellite remote sensing and application.

Ailin Liang received the B.S. degree in GIS from Northeast Forestry University, Haerbin, China, in 2013, and the Ph.D. degree in photogrammetry and remote sensing from Wuhan University, Wuhan, China in 2018.

She is currently working with the School of Remote Sensing and Geomatics Engineering, Nanjing University of Information Science and Technology. Nanjing, China. Her research interests include atmospheric remote sensing, atmospheric greenhouse gas remote sensing monitoring, atmospheric LIDAR remote sensing detection, climate change, carbon cycle, etc.

Wei Gong received the B.S. degree in photonics engineering from the Huazhong University of Science and Technology (HUST), Wuhan, China, in 1993, the M.S. degree in electronics from the Chinese Academy of Science, Lanzhou, China, in 1996, and the Ph.D. degree in physical electronics from HUST, Wuhan, in 1999.

He is currently a Professor and Dean with the Electronic Information School, Wuhan University. His research interests include teaching and research of new laser, optical technology, and its remote sensing applications, and has made achievements in atmospheric soundings of LIDAR and optical remote sensing.